

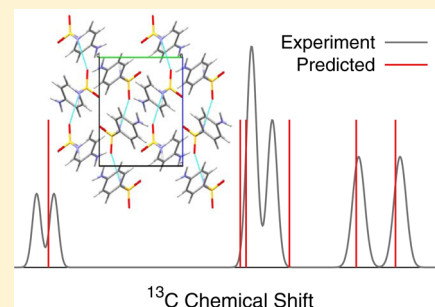
Fragment-Based Electronic Structure Approach for Computing Nuclear Magnetic Resonance Chemical Shifts in Molecular Crystals

Joshua D. Hartman and Gregory J. O. Beran*

Department of Chemistry, University of California, Riverside, California 92521, United States

S Supporting Information

ABSTRACT: First-principles chemical shielding tensor predictions play a critical role in studying molecular crystal structures using nuclear magnetic resonance. Fragment-based electronic structure methods have dramatically improved the ability to model molecular crystal structures and energetics using high-level electronic structure methods. Here, a many-body expansion fragment approach is applied to the calculation of chemical shielding tensors in molecular crystals. First, the impact of truncating the many-body expansion at different orders and the role of electrostatic embedding are examined on a series of molecular clusters extracted from molecular crystals. Second, the ability of these techniques to assign three polymorphic forms of the drug sulfanilamide to the corresponding experimental ^{13}C spectra is assessed. This challenging example requires discriminating among spectra whose ^{13}C chemical shifts differ by only a few parts per million (ppm) across the different polymorphs. Fragment-based PBE0/6-311+G(2d,p) level chemical shielding predictions correctly assign these three polymorphs and reproduce the sulfanilamide experimental ^{13}C chemical shifts with 1 ppm accuracy. The results demonstrate that fragment approaches are competitive with the widely used gauge-invariant projector augmented wave (GIPAW) periodic density functional theory calculations.



1. INTRODUCTION

The sensitivity of chemical shielding tensors to the local chemical environment makes solid-state nuclear magnetic resonance (NMR) measurements a valuable complement to X-ray and neutron scattering techniques for studying molecular crystals. Moreover, solid-state NMR measurements do not require large, pure single crystals, and they can even be performed in situ. For these reasons, the combination of powder X-ray diffraction, which readily provides information regarding the long-range order of a crystal (e.g., space group and lattice parameters), and NMR to determine local packing configurations has proved a particularly potent combination for solving crystal structures.^{1–3}

In practice, NMR molecular crystal studies rely heavily on computational predictions for the chemical shifts of putative structures to assign and interpret the experimental spectrum. At present, these calculations are most often performed using the periodic density functional theory (DFT)-based gauge-including projected augmented wave (GIPAW) approach.⁴ GIPAW techniques have been used successfully in many different crystallographic applications, as discussed in recent reviews.^{5,6}

This success does involve a degree of fortuitous error cancellation, however. As demonstrated by benchmark studies, isotropic ^{13}C chemical shifts computed with various DFT functionals deviate from coupled cluster singles and doubles with perturbative triples (CCSD(T)) shifts by ~ 4 – 5 ppm.^{7,8} Similar errors are often observed with respect to experimental ^{13}C shifts.^{9,10} Such errors exceed the couple ppm variations in the ^{13}C chemical shifts that distinguish polymorphic molecular crystals such as sulfanilamide¹¹ or naproxen.¹²

On the other hand, correlated wave function methods like second-order Møller–Plesset perturbation theory (MP2) or coupled cluster singles and doubles (CCSD) can perform better, with errors of only ~ 2 ppm relative to CCSD(T) benchmarks.^{7,8} Similar improvements are observed with these methods for other NMR-active nuclei as well.

MP2 and coupled cluster calculations for periodic crystals are computationally demanding, even when local correlation approximations are employed. Linear-scaling^{13–16} and other efficient algorithms^{17,18} for calculating NMR chemical shifts can be applied to large, nonperiodic clusters, but the computational prefactor remains high. Fragment-based electronic structure methods, on the other hand, make it feasible to apply high-level electronic structure methods to pharmaceuticals and other interesting molecular crystals. For example, these techniques have been used to explain the near degeneracy of the two polymorphs of aspirin,¹⁹ to sort out the relative stabilities of the five known oxalyl dihydrazide polymorphs,²⁰ to resolve controversy surrounding ice Ih²¹ to assign the vibrational spectra of solid formic acid polymorphs,²² to examine the phase diagram of carbon dioxide,²³ and other examples.^{24–26} Hybrid density functional methods also sometimes out-perform semilocal functionals for NMR shielding calculations.^{7,8} Fragment methods enable the routine use of Gaussian-type orbital basis sets which make the use of hybrid density functionals much more computationally feasible than in planewave basis sets.

Received: August 19, 2014

Published: October 24, 2014



In this work, we apply such fragment methods to molecular crystals, with an eye toward using NMR to discriminate among different crystal polymorphs. In particular, we utilize a many-body expansion approach that decomposes the chemical shielding tensor contributions for a given molecular in a crystal into monomers, their pairwise interactions, 3-body interactions, etc. Given the widespread use of GIPAW DFT in the field, our study here focuses on DFT methods. Future works will examine the impact of using correlated wave function methods.

We are not the first to utilize a fragment approach to compute NMR chemical shielding calculations. Various fragment strategies have been applied to large biomolecules, for instance.^{27–33} Similarly, an assortment of electrostatic embedding methods have been used to mimic the effect of the crystal lattice on the chemical shielding of a monomer, including techniques such as the embedded-ion method (EIM)³⁴ or the surface charge representation of the electrostatic embedding potential (SCREEP) model.³⁵ Such models may also employ a small cluster of nearest-neighbor monomers to capture their influence on the chemical shielding tensors. Multilevel QM/QM and QM/MM schemes have also been used,^{36–40} including ones in the context of linear-scaling techniques.

This study addresses several key questions surrounding the use of fragment-based NMR calculations in the context of molecular crystals. First, how rapidly does the many-body expansion for the chemical shielding tensors converge? Second, what is the role of electrostatic embedding, and what is the appropriate representation for this embedding potential? Are point charges sufficient? Should one also include polarizable dipoles in the embedding potential? These questions are investigated using calculations on a series of molecular clusters extracted from experimental crystal structures.

Third, can such a fragment approach accurately discriminate among the NMR spectra for different molecular crystal polymorphs? In particular, we demonstrate that employing a fragment approach with the hybrid Perdew–Burke–Ernzerhof (PBE0) density functional allows one to correctly assign the isotropic chemical shifts for three crystal polymorphs of the antibacterial agent sulfanilamide. The subtle differences in the chemical shifts among polymorphs make this a particularly challenging example, and we demonstrate that the accuracy of the results obtained for sulfanilamide with the hybrid PBE0 functional is notably improved compared to those from the nonhybrid PBE functional.

2. THEORY

2.1. Many-Body Expansion for Ab Initio Shielding Tensor Calculations. The many-body expansion decomposes the energy of a set of interacting molecules into a series of 1-body, 2-body, and higher-order contributions,

$$E_{\text{total}} = \sum_i E_i + \sum_{i,j} \Delta^2 E_{ij} + \sum_{i,j,k} \Delta^3 E_{ijk} + \dots \quad (1)$$

where E_i is the energy of the i -th monomer, $\Delta^2 E_{ij}$ is the interaction energy between the pair of monomers i and j , $\Delta^2 E_{ij} = E_{ij} - E_i - E_j$, and $\Delta^3 E_{ijk}$ is the 3-body contribution to the interaction energy given by $\Delta^3 E_{ijk} = E_{ijk} - \Delta^2 E_{ij} - \Delta^2 E_{ik} - \Delta^2 E_{jk} - E_i - E_j - E_k$. The sums here run over only unique dimers, trimers, etc.

The many-body expansion is formally exact, but in practice it is useful only when some approximation or truncation is employed. Much previous research demonstrates that 1- and 2-body terms typically dominate the energy, but the 3-body and higher terms

describe many-body polarization and dispersion effects which generally should not be neglected. They often account for 10–20% of the lattice energy of a crystal and are critical to determining the relative stabilities of different crystal polymorphs.^{41–44}

These higher-order terms can either be computed explicitly, which is computationally demanding, or approximated (e.g., using a polarizable force field as in our hybrid many-body interaction approach^{45–47}). Alternatively, employing an electrostatic embedding potential in the calculation of the 1- and 2-body terms helps capture the polarization effects, thereby reducing the importance of the higher-order terms in the many-body expansion and allowing one to truncate the series at lower orders.

For a given nucleus A , the NMR chemical shielding tensor can be calculated as the second derivative of the electronic energy with respect to the i -th component of the external magnetic field B_i and the j -th component of the nuclear magnetic moment of interest μ_j^A :

$$\sigma_{ij}^A = \frac{\partial^2 E}{\partial B_i \partial \mu_j^A} \quad (2)$$

The gauge problem, which results from the appearance of the external magnetic field in the Hamiltonian as a vector potential without a fixed origin, can be overcome using so-called gauge-including atomic orbitals (GIAOs).^{48,49}

The many-body expansion is a linear function, and derivatives of the total energy can be written as derivatives of the individual n -body contributions.^{22,50} Therefore, the exact shielding tensor in a cluster/crystal can be written as

$$\sigma_{\text{total}} = \sum_i \sigma_i + \sum_{i,j} \Delta^2 \sigma_{ij} + \sum_{i,j,k} \Delta^3 \sigma_{ijk} + \dots \quad (3)$$

Once again, approximations to this expansion need to be employed in practice. Approximating the higher-order terms using a lower level of theory can be problematic. For example, one cannot readily obtain shielding tensors from derivatives of the sort given in eq 2 for a polarizable force field. In the standard energy-based many-body expansion, Hartree–Fock (HF) theory often provides a good approximation for the higher-order terms when paired with more accurate electronic structure methods for the 1- and 2-body terms.^{51–55} However, significant differences in the absolute shielding tensor values between different electronic structure methods (e.g., Hartree–Fock vs DFT or MP2) hinders this approach.

For these reasons, truncating the many-body expansion at a given order proves more effective. In a periodic crystal, the 1-body terms sum over monomers in the (asymmetric) unit cell. The higher-order terms involve at least one molecule in the unit cell, while the other partner molecule(s) may either lie within the central unit cell or in periodic image cells. Distance-based criteria are used to include only contributions within a given radius of the central unit cell monomer(s). For reasons of practical computational cost, one aims to truncate the series at 2-body or 3-body terms. The computational effort required to calculate higher-order terms grows rapidly, and a summation over large numbers of small n -body contributions can be plagued by numerical precision issues. Electrostatic embedding may help reduce the error arising from truncation by incorporating higher-order polarization effects into lower-order many-body terms (see Section 2.2).

Fragmentation of a cluster/crystal has the distinct computational advantage of reducing the cost of a given calculation to

approximately the cost of the largest n -body fragment multiplied by the number of such fragments in the system. These computational savings become increasingly important for higher order post-HF correlation methods, which scale $O(N^5)$ or worse with system size N . Furthermore, the fragment approach benefits from the inherent parallelizability that results from breaking the problem into a series of small components.

2.2. Electrostatic Embedding. Electrostatic embedding is widely used to capture some higher-order polarization effects in low-order truncated many-body expansions.^{22,34,35,54,56–59} Such polarization effects play a critical role in determining the local nuclear shielding and therefore are critical to NMR chemical shift calculations.

Embedding models range from simple point charges to fully self-consistent electron densities. Within the framework of both the SCREEP and embedded ion methods, the Madelung potential experienced by a given molecule inside an infinite crystal lattice is approximated through the use of an optimized set of point charges. Specifically, the SCREEP method reproduces the Madelung potential through an iterative fitting procedure using a collection of point charges placed on a grid positioned at the van der Waals radius of the molecule of interest.³⁵ The EIM uses a similar fitting procedure, but it places the fitted charges at the atomic centers of molecules in a collection of adjacent unit cells.³⁴

Here, we choose a straightforward embedding approach based on distributed multipole analysis (DMA)^{60–62} computed for each unique monomer in the unit cell from DFT densities. Tan and Bettens have similarly adopted distributed multipole embedding in their NMR calculations on biomolecules.³³ Point multipoles are then placed at atomic centers for molecules within a user-chosen distance of the monomer of interest in the central unit cell.

One could compute the Ewald potential from the infinite lattice of distributed multipole moments, and then fit a finite set of corresponding point multipoles as in SCREEP or EIM, but in practice, the impact of the embedding potential on the computed chemical shifts appears to converge within a radius of 15–20 Å, at least for neutral molecular crystals (see Supporting Information). Therefore, we simply surround the molecule(s) of interest with a sufficiently large sphere of embedding multipoles.

The simplest embedding model truncates the multipole expansion at point charges. The next logical step would be to include dipoles. Dipole polarization effects are often important in molecular crystals,⁴¹ so one should embed using both permanent and induced dipole contributions. The induced multipoles used here are computed using a periodic distributed multipole/distributed polarizability model^{63,64} that has been used successfully in our ab initio force field^{47,65} for fragment-based molecular crystal energy calculations.^{19,20,42} The t -th induced multipole moment ΔQ_t^A on atom A is due to multipole moments on atom B is computed according to

$$\Delta Q_t^A = - \sum_{t'u} \alpha_{tt'}^A T_{t'u}^{AB} (Q_u^B + \Delta Q_u^B) \quad (4)$$

where $\alpha_{tt'}^A$ is the static polarizability tensor on atom A and the $T_{t'u}^{AB}$ matrix includes the distance- and orientation-dependent contributions for the interaction of two different spherical tensor multipole moment components on atoms A and B .⁶⁶ An empirical Tang–Toennies damping function⁶⁷ is applied to the $T_{t'u}^{AB}$ to avoid the “polarization catastrophe” at short-range.⁶⁶ The crystalline induced multipole moments used here are computed

self-consistently among all molecules in a large, finite cluster as described previously.⁴⁷

The total (permanent plus induced) dipole moments are subsequently used to embed the monomer and dimer fragment calculations. The dipole embedding potential is constructed by placing a set of two point charges separated by 0.01 Å for each dipole moment on each atom center.²² The chemical shielding tensors obtained prove insensitive to the separation of the point charges used to mimic the dipole moment. Calculations on an acetamide cluster which increased the point charge separation 4-fold to 0.04 Å altered the computed chemical shifts by less than 0.01 ppm.

Overall, this approach provides a useful crystalline electrostatic embedding environment, which can be systematically improved through the inclusion of higher-order permanent and induced multipole terms. As will be discussed in the results below, however, there appears to be little need for including such higher-order terms in practice, at least for neutral organic crystals.

Figure 1 summarizes the model for crystals. One calculates the monomer (1-body) shielding tensor for each symmetrically

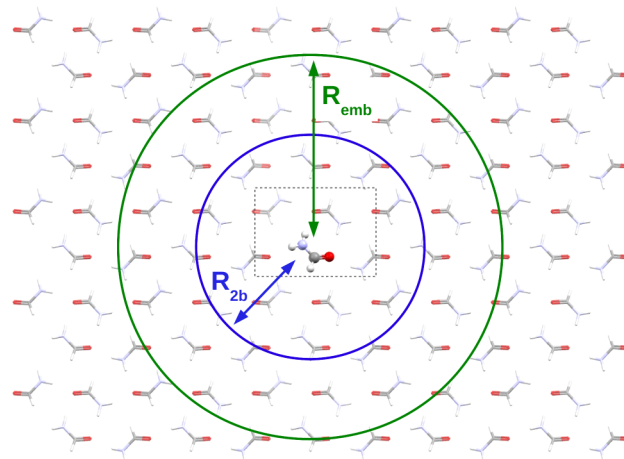


Figure 1. Schematic of the crystalline fragment approach. The molecule in the asymmetric cell is highlighted, and the distances R_{2b} and R_{emb} specify the cutoffs for the 2-body interactions and the point charge embedding, respectively.

unique monomer in the unit cell. Two-body contributions from pairwise interactions within a user-specified cutoff radius R_{2b} of the central molecule(s) are computed explicitly, and electrostatic embedding is optionally included out to a cutoff of R_{emb} .

In the following sections, we will analyze the interplay between the rank of the many-body expansion used and the role of the electrostatic embedding model on the predicted chemical shielding tensors. In practice, one must choose (1) the cutoff distance(s) for including explicit 2-body and perhaps 3-body terms, (2) the rank of the multipoles used to construct the embedding environment (no embedding, point charge embedding, or point charge plus dipolar embedding), and (3) the cutoff distance defining the radius of the embedding environment.

3. COMPUTATIONAL METHODS

3.1. Theoretical Techniques. The many-body fragmentation was carried out using our hybrid many-body interaction (HMBI) code.^{43–47} The ab initio shielding tensor calculations for each fragment were performed using Gaussian09⁶⁸ with the hybrid PBE0 hybrid density functional⁶⁹ the 6-311++G**

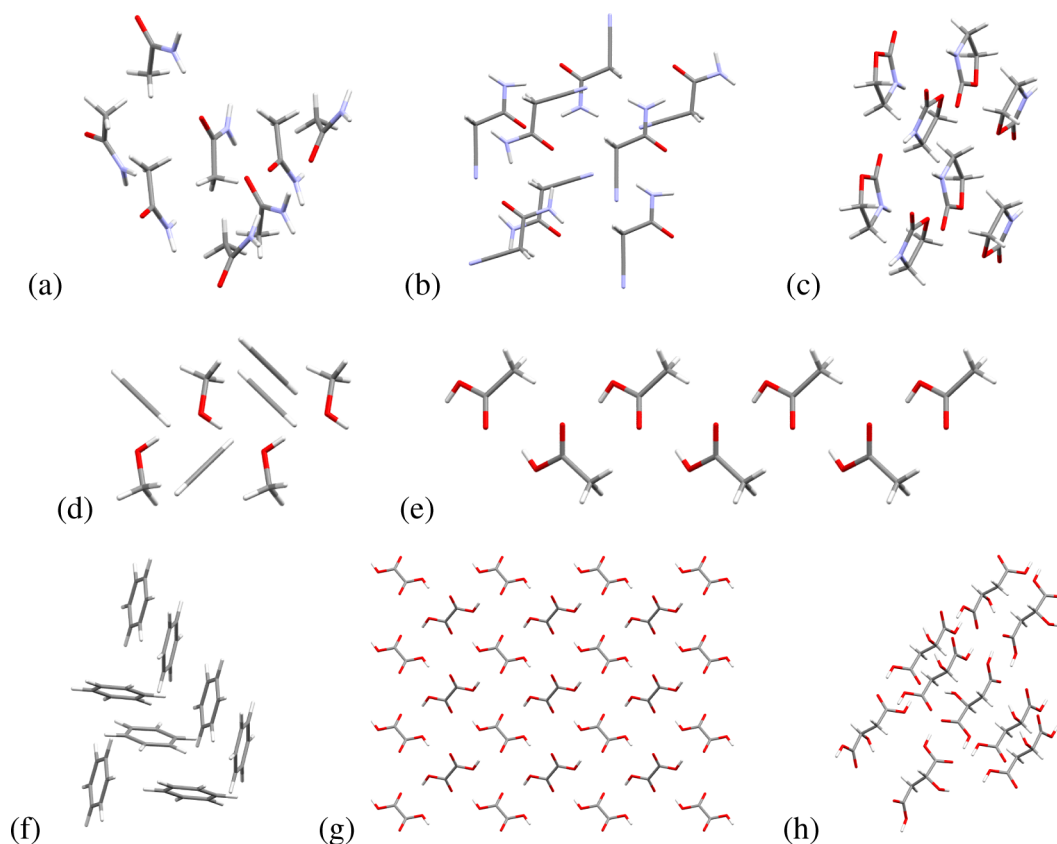


Figure 2. Selected molecular clusters from the benchmark set. (a) acetamide, (b) cyanoacetamide, (c) 2-oxazolidinone, (d) methanol/ethyne, (e) acetic acid 1-D chain, (f) benzene, (g) oxalic acid 2-D sheet, (h) malic acid 3-D cluster.

(clusters) or 6-311+G(2d,p) (sulfanilamide) basis sets^{70–73} in the GIAO approximation. Point-group symmetry was turned off for each fragment calculation to preserve the proper orientation of each fragment. This is important because the fragmentation expansion is expressed here in terms of the full chemical shielding tensors, not just the isotropic component. A large DFT integration grid consisting of 150 radial and 974 Lebedev angular points was used to provide near-rotational invariance, thereby minimizing noise introduced in the chemical shielding tensors for symmetrically equivalent molecules which occur with different orientations in different fragments.

The distributed multipoles and polarizabilities used to construct the embedding environment were computed with either CamCasp 5.6⁷⁴ or the stand-alone GDMA package^{62,75} using the asymptotically corrected^{76,77} PBE0 density functional in the aug-cc-pVTZ basis set.⁷⁸ For sulfanilamide, the more compact Sadlej triple- ζ basis^{79,80} set was used instead. Previous experience suggests that these two basis sets provide similar multipole moments and polarizabilities.^{80,81} The induced multipoles were obtained in a finite cluster that included all molecules within 15 Å of any molecule in the central unit cell using a nearest-atom criterion. A damping parameter of $\beta = 1.4$ au was employed in the Tang–Toennies damping function, which has proved to be a reasonable value for a variety of organic molecular crystals.^{19,20,47,81} See previous descriptions of the ab initio force field used in our hybrid many-body interaction model for further details.^{47,81}

In the benchmark finite clusters, point charges were placed on the atoms of all molecules not directly involved in a given n -body term. In the periodic crystals, point charges were placed on all molecules lying within 30 Å of the symmetrically unique

monomer in the central unit cell. One should note, however, that the chemical shifts are already mostly converged by 15 Å (see Supporting Information). Once the chemical shielding tensor σ_{ij} has been computed for each atom via the many-body expansion, it is symmetrized and diagonalized to obtain principal components σ_{11} , σ_{22} , and σ_{33} . The isotropic shielding tensor σ_{iso} is computed as the average of the three principle components.

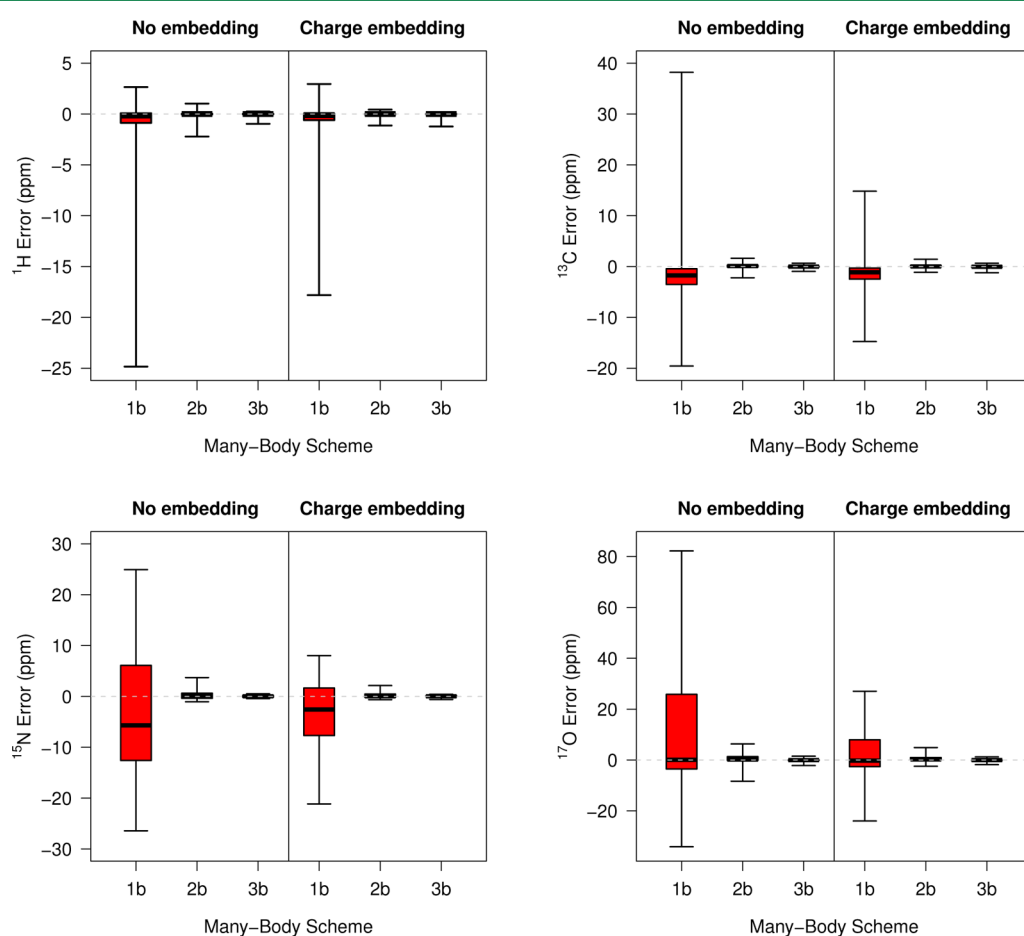
Finally, GIPAW NMR calculations for three sulfanilamide polymorphs were performed with the PBE exchange-correlation functional⁸² using CASTEP⁸³ at the same crystal geometries as above.⁸⁴ Ultrasoft pseudopotentials were generated on the fly, and convergence in the NMR isotropic shielding values to within a small fraction of a ppm was achieved using a planewave cutoff of 850 eV and a $3 \times 3 \times 3$ k-point grid (see Supporting Information).

3.2. Crystal Structures. All structures used here were obtained from the Cambridge Structure Database maintained by the Cambridge Crystallographic Data Center (CCDC). CCDC reference codes for each structure used are provided in parentheses below. First, a series of benchmark NMR calculations were performed using 13 clusters extracted from experimental crystal structures. The test set was chosen to include a variety of intermolecular interactions, ranging from hydrogen-bonded crystals to van der Waals dispersion-bound crystals.

The test set includes ten dense octamer clusters consisting of acetamide (ACEMID05), acetic acid (ACETAC07), acetonitrile (QQQCIV01), benzene (BENZEN06), formaldehyde (KEMZIL01), cyanoacetamide (CYANAC), imidazole (IMAZOL06), methanol-ethyne clathrate (CIYYEP), oxalic acid (OXALAC04), and 2-oxazolidinone (OXAZIL01). Given the importance of polarization effects, three additional clusters were constructed to focus on polarization effects in hydrogen bonding networks: a

Table 1. Root-Mean-Square Errors in the Isotropic Chemical Shieldings (in ppm) Introduced by the Fragment Approach with Different Embedding Models at the PBE0/6-311++G** Level^a

atom type	1-body			2-body			3-body		
	none	charge	dipole	none	charge	dipole	none	charge	dipole
¹ H (all) [436]	4.83	3.66	3.13	0.29	0.16	0.12	0.14	0.17	0.23
¹ H (no H-bond) [366]	1.32	0.84	0.85	0.12	0.08	0.10	0.06	0.06	0.06
¹ H (H-bond) [70]	11.68	8.93	7.56	0.68	0.35	0.21	0.33	0.42	0.56
¹³ C (all) [304]	6.98	4.19	4.92	0.41	0.30	0.40	0.23	0.26	0.34
¹⁵ N (all) [56]	13.20	7.65	5.35	0.90	0.55	0.51	0.22	0.17	0.27
¹⁵ N (no H-bond) [28]	7.06	2.87	4.78	0.46	0.33	0.46	0.20	0.14	0.23
¹⁵ N (H-bond) [28]	17.28	10.43	5.87	1.19	0.71	0.56	0.24	0.20	0.31
¹⁷ O (all) [248]	24.95	9.69	11.48	1.98	1.20	1.39	0.40	0.36	0.56
¹⁷ O (no H-bond) [128]	7.61	3.76	8.51	0.95	0.51	0.72	0.30	0.25	0.27
¹⁷ O (H-bond) [120]	35.00	13.37	13.97	2.67	1.64	1.86	0.49	0.45	0.76

^aThe number in square brackets indicates the number of data points for each atom type in the test set.**Figure 3.** Distribution of errors in the H/C/N/O isotropic shielding tensors (in ppm) due to fragmentation for the 13 test clusters at the PBE0/6-311++G** level. The colored boxes include the middle 50% of the errors, the solid line marks the median error, and the whiskers indicate the maximum errors.

one-dimensional hydrogen-bonded chain of seven acetic acid molecules (ACETAC07), a two-dimensional sheet consisting of 25 hydrogen bonded oxalic acid molecules (OXALAC06), and a 9-molecule, three-dimensional cluster of malic acid consisting of eight molecules hydrogen bonded around a central molecule (DLMALC11).

Note that the experimental crystal geometries for this test set were used as-is, without any geometry optimization. Because we only compare fragment calculations against fully quantum ones, rather than against experimental shifts, errors in locations of the

hydrogen atoms or other minor experimental errors do not represent a significant problem. Selected clusters from the test are pictured in Figure 2. Images of the remaining clusters and Cartesian coordinates for all the clusters are provided as Supporting Information.

Second, the fragment approach was used to assign room-temperature experimental ¹³C NMR spectra for three different polymorphs of sulfanilamide. Room-temperature experimental structures for the α (SULAMD05), β (SULAMD06), and γ (SULAMD02) polymorphs were optimized using the dispersion-

corrected B3LYP-D* density functional^{85,86} and the TZP basis set,⁸⁷ as implemented in Crystal09.^{88,89} The positions of all atoms were relaxed, while the lattice parameters were fixed at their experimental values to capture the thermal expansion of the crystal at room temperature that would otherwise be missed in a 0 K geometry optimization. The optimized sulfanilamide structures are also provided as Supporting Information.

4. RESULTS AND DISCUSSION

In this section, we first benchmark the performance of the fragment approach with and without electrostatic embedding against conventional NMR shielding calculations for the 13 test clusters. We examine how the rate of convergence of the many-body expansion varies without any electrostatic embedding, with a simple point-charge embedding model, and with an embedding environment including both point charges and polarizable dipoles. These test clusters enable us to assess the impact of hydrogen bonding, van der Waals dispersion, aromatic ring currents, and other intermolecular interactions on the accuracy of the fragment approach.

Second, as a challenging example of NMR crystallography, the fragment approach is applied to assign three crystal polymorphs of the drug sulfanilamide based on matching the predicted and experimental ¹³C isotropic chemical shifts. The fragment results for sulfanilamide are also compared against those obtained with widely used periodic GIPAW DFT techniques.

4.1. Benchmark Calculations on Molecular Clusters. We first examine the effects of truncating the many-body representation of the chemical shielding tensor elements for a test set of molecular clusters which include a variety of intermolecular interactions. The truncated many-body expansion calculations (with or without electrostatic embedding) for the isotropic chemical shieldings, the anisotropy, and asymmetry (Supporting Information) are compared against benchmark calculations on the entire cluster at the same level of theory.

As illustrated in Table 1 and Figure 3, a simple 1-body model for the isotropic chemical shieldings performs poorly, because it omits all effects of the neighboring molecules on the chemical shifts. Including 2-body terms in the many-body expansion significantly reduces the error, bringing the root-mean-square (rms) errors in the isotropic chemical shieldings below 1 ppm for hydrogen, carbon and nitrogen. Oxygen has a larger rms error of 2 ppm, but it still represents a dramatic improvement over the 1-body model error of 25 ppm. If 3-body terms are also included, the errors decrease further, particularly for nitrogen and oxygen, which are more sensitive to environmental effects. At the 3-body level, all four types of nuclei exhibit subppm root-mean-square errors relative to the full system calculations.

Consider next the role of electrostatic embedding. As shown in Table 1, electrostatic embedding provides substantial improvement at the 1-body level. Including point charge embedding reduces the root-mean-square errors 25–60%. Additionally, including polarizable dipoles moderately improves the results further in several cases. However, the errors in 1-body embedding models remain up to an order of magnitude larger than those obtained with a nonembedded 2-body model.

Embedding proves less important at the 2-body level. For carbon and hydrogen, charge embedding has relatively little effect on the isotropic shieldings. For oxygen and nitrogen, however, it does prove useful. Surprisingly, the results of the dipolar embedding model are often worse than those obtained with charge embedding. At the 3-body level, electrostatic embedding provides no consistent beneficial impact. Of course, the

molecules in the clusters examined here are all neutral. Embedding may be more important if charged functional groups or molecules were present, as is the case in ionic crystals or in many biomolecules.

In addition to the isotropic chemical shifts, NMR shielding tensors provide information regarding the NMR line shapes. Several different conventions exist for relating the tensors to the line shape, such as the Haeberlen–Mehring–Spiess convention.^{90–92} These various metrics are typically expressed in terms of the principal components of the shielding tensor. As shown in the Supporting Information, the fragment approximations and electrostatic embedding models behave similarly well for the individual principal components as they do for the isotropic components. In other words, measures such as the anisotropy or asymmetry of the shielding tensor can be computed reliably using a fragment approach as well.

Examination of the isotropic shielding error box plots in Figure 3 indicates that while most of the errors arising from fragmentation are small, there are some significant outliers. Not surprisingly, these larger errors often arise on atoms involved in hydrogen bonding. Table 1 partitions the statistical errors for the H/N/O atom types according to whether or not the atoms directly participate in a hydrogen bond, and Table 2 reports the

Table 2. Cluster-by-Cluster Root-Mean-Square Errors (in ppm) Introduced in the PBE0/6-311++G(d,p) Isotropic Shifts by Using the 2-Body Plus Charge Embedding Fragment Model

crystal	RefCode	hydrogen	carbon	nitrogen	oxygen
acetamide	ACEMID05	0.03	0.21	0.41	0.90
acetic acid	ACETAC07	0.02	0.15		0.65
acetonitrile	QQQCIV01	0.02	0.30	0.31	
benzene	BENZEN06	0.05	0.44		
formaldehyde	KEMZIL01	0.01	0.07		0.19
cyanoacetamide	CYANAC	0.06	0.15	0.84	1.03
imidazole	IMAZOL06	0.06	0.31	0.46	
methanol-ethyne clathrate	CIYYEP	0.04	0.13		0.89
oxalic acid	OXALAC04	0.14	0.26		2.07
2-oxazolidinone	OXAZIL01	0.04	0.15	0.18	0.80
1-D acetic acid 7-mer	ACETAC07	0.41	0.67		0.03
2-D oxalic acid sheet	OXALAC06	0.31	0.29		0.89
3-D malic acid cluster	DLMALC11	0.09	0.19		1.54
overall		0.16	0.30	0.55	1.20

errors separately for each cluster. Involvement in a hydrogen bond dramatically increases the errors in a 1-body truncation model. At the 2- and 3-body level, the errors for the hydrogen bonding atoms remain larger than those of non-hydrogen bonding atoms, but the overall errors are much smaller than at the 1-body level. Electrostatic embedding behaves similarly as before, though with a slightly larger effect on hydrogen bonded atoms, as might be expected due to the role of polarization.

Aromatic ring currents represent another class of interactions that might be difficult to model with a fragment approach. For example, QM/MM calculations on hexa-peri-hexabenzocoronene clusters demonstrate long-range correlation contributions to chemical shielding that are not captured by point charge embedding.³⁹ In the fragment approach used here, however, those longer-range correlation terms between molecules are

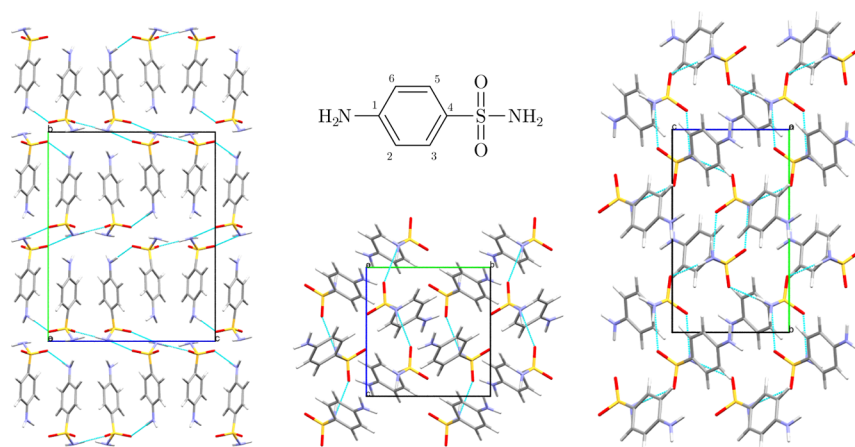


Figure 4. α (left), β (bottom center), and γ (right) polymorphs of sulfanilamide. The carbon atom numbering is also indicated (top center).

included in a pairwise or 3-body fashion, which appears to work well. The rms errors for the ^{13}C isotropic shifts in the benzene cluster tested here is 0.44 ppm at the 2-body plus charge embedding level. This error is moderately worse than the 0.30 error obtained for all carbons in the test set (Table 2), but it is well within the inherent DFT model errors and is much smaller than the errors obtained by neglecting those longer-range correlations.

Overall, these results indicate that the many-body expansion behaves well, with the inclusion of higher-order terms leading to smaller errors. Furthermore, the reduction in errors afforded through the inclusion of 3-body terms is much less significant than the 2-body contributions, suggesting that 3-body and higher terms can often be ignored. Charge embedding can be useful, particularly for oxygen/nitrogen nuclei, but polarizable dipolar embedding does not appear to provide significant improvements over charge embedding if 2-body or higher interactions are included.

The inherent errors in DFT isotropic chemical shifts relative to experiment are typically several ppm for carbon and a couple tenths of a ppm for hydrogen for organic compounds.⁹ Thus, the errors introduced by fragmentation are on par with or smaller than the errors expected from the underlying model chemistry. From this perspective, a model including up to 2-body interactions with point-charge embedding may perform well for many chemical applications and significantly reduced computational cost.

4.2. Assigning the Polymorphs of Sulfanilamide. Having verified the efficacy of a many-body fragment-based approach to NMR chemical shielding tensor calculations in the model clusters above, we now turn our attention to the reproduction of the isotropic chemical shifts obtained from cross-polarization magic angle spinning (CP/MAS) ^{13}C NMR experiments for the α , β , and γ polymorphs of the antibacterial agent sulfanilamide.¹¹ The structure of a fourth δ polymorph has been reported,⁹³ but to our knowledge, NMR data for this fourth form is not currently available. ^{15}N shifts for the three primary forms have also been measured experimentally, but dynamics in the sulfa group appear to play an important role in their values.¹¹ The proper treatment of such dynamical effects is beyond the scope of this study, so we do not examine the nitrogen shifts further.

The intramolecular conformation adopted by sulfanilamide is very similar across the α , β , and γ forms, but the intermolecular hydrogen bonding patterns differ (Figure 4). Accordingly, the NMR spectra are similar for all three forms, with ^{13}C shifts varying by only a couple ppm among these three polymorphs (see

Table 3) The shifts in the ~ 115 (C2 and C6) and ~ 130 ppm (C3, C4, and C5) regions provide key fingerprints for identifying the different forms.

Table 3. Experimental¹¹ and the 2-Body Plus Point Charge Embedding Predicted PBE0/6-311+G(2d,p) ^{13}C Isotropic Chemical Shifts (ppm) for Three Polymorphs of Sulfanilamide^a

polymorph	C1	C3/C5	C4	C2/C6
α (expt)	153.7	128.3	128.0	115.3, 113.1
α (calc)	151.7	128.7, 128.0	129.0	114.5, 113.0
β (expt)	153.4	129.5	127.1	117.1, 112.3
β (calc)	153.0	130.1, 130.8	128.0	117.5, 113.0
γ (expt)	151.0	129.6	127.1	115.1, 112.7
γ (calc)	152.5	129.7, 128.7	128.7	114.8, 112.1

^aThe atom numbering corresponds to that shown in Figure 4. C3 and C5 exhibit slightly distinct shifts in the calculations, but they appear as a single peak experimentally due to dynamical averaging.

Fragment-based NMR chemical shielding calculations were performed at the 1- and 2-body levels with and without charge embedding. Test calculations found no significant advantage to including polarized dipolar embedding, consistent with the results on the smaller clusters. All three polymorphs have a single molecule in the asymmetric unit cell, and the chemical shieldings were computed for this molecule.

Two-body interactions involving all molecules lying within 12 Å of the central unit cell molecule (defined by the shortest interatomic distance between the two molecules) were included. Electrostatic embedding was included by placing point charges on all molecules lying within 30 Å of the central unit cell molecule that are not involved in a particular monomer or dimer calculation. Empirical testing suggests that the 2-body and embedding contributions are well-converged with these cutoff distances (see Supporting Information).

When comparing against experiment, the computed absolute isotropic shieldings σ_{iso} must be properly referenced to obtain relative isotropic chemical shifts δ_{iso} . This can be done by comparing the computed shieldings against those from a reference compound (e.g., adamantane),⁹⁴ by using empirical linear scaling regressions of the form

$$\delta_{\text{iso}} = a\sigma_{\text{iso}} + b \quad (5)$$

which have been determined by comparing measured shifts with those computed using the same level of theory on large numbers of molecules,⁹ or by performing such a regression “internally” against measured shifts only from the system in question. In either of the linear regression approaches, the slope a should ideally be -1 (corresponding to a straightforward relative shift b), but in practice, it may deviate from that value by a few percent due to errors in the model chemistry.

Here, we adopt the internal referencing approach. Specifically, with an eye toward future NMR crystallography applications where the actual crystal structures are unknown and one has a theoretical set of candidate structures, we ask the following question: If we pretend that the polymorph structure corresponding to each of the three experimental spectra were not known, could we correctly assign the three structures based on the calculated spectra? Accordingly, there are six possible ways to assign the three calculated spectra to the experimental ones to identify the polymorphs.

For a given choice of assignment, there are six computed ^{13}C isotropic shifts per polymorph, or a total of 18 shifts across all three polymorphs. We perform a linear regression of the form given in eq 5 to fit the 18 computed shifts to the corresponding experimental ones. Note that the C3 and C5 shifts differ slightly in the computations, but they are experimentally indistinguishable (due to the aforementioned dynamics associated with the sulfa group).¹¹ We also considered using only the 15 unique shifts (averaging the predicted C3 and C5 shieldings), but this had little impact on the accuracy of the resulting fits, so we will not discuss it further.

The linear regressions were performed separately for each of the six possible polymorph assignments, and the root-mean-square error between the computed and experimental isotropic shifts were compared. This entire procedure was repeated for both the 1-body and 2-body models with and without point charge embedding. Details of the fits are provided in Supporting Information.

The corresponding root-mean-square errors are plotted in Figure 5. Without embedding, the 1-body methods performs

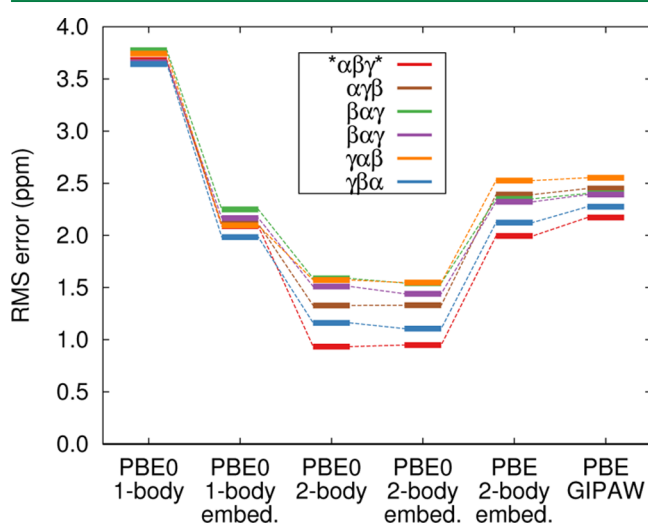


Figure 5. Errors between the calculated and experimental chemical shifts for the six possible sulfanilamide polymorph assignments using both fragment and GIPAW approaches. Fragment results are presented both with and without charge embedding. The correct assignment is $\alpha\beta\gamma$ (red).

poorly. The root-mean-square errors approach 4 ppm for all six assignments, and there is very little discrimination among any of the possible assignments. This result is unsurprising, since the differences among the polymorphs are primarily intermolecular rather than intramolecular. Including point charge embedding at the 1-body level reduces the root-mean-square errors down to ~ 2 ppm, but it still does not identify the correct polymorph assignment.

Substantial improvements are obtained by including 2-body contributions. Notably, the level of discrimination is improved in the sense that larger differences in the root-mean-square errors are observed for the different possible assignments. More importantly, the correct polymorph assignment exhibits the smallest rms error relative to experiment. Charge embedding provides no appreciable improvement at the 2-body level, which is consistent with the results seen for carbon atoms in the test clusters discussed above. The slopes of -0.97 to -0.98 in the linear regression (eq 5) for the correct polymorph assignment are close to the ideal value of -1 for the 2-body models, compared to only -0.91 for the 1-body models (see Supporting Information). Overall, the 2-body models with the correct assignment reproduce the experimental shifts within ~ 1 ppm rms error.

The stick spectra in Figure 6 provide a visual assessment of role of 2-body contributions. Most notably, the qualitative trends for

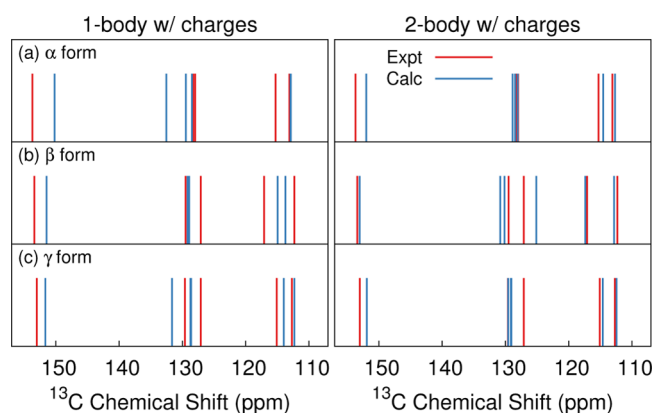


Figure 6. Stick spectra comparing the predicted PBE0/6-311+G(2d,p) and experimental isotropic shifts for sulfanilamide using 1-body and 2-body models with charge embedding. The 2-body model captures the qualitative trends in the 115 and 130 ppm regions much better than the 1-body model.

these three polymorphs in the ~ 115 and ~ 130 ppm regions are poorly described at the 1-body with charge embedding level, while the corresponding 2-body model performs much better.

Although the 2-body models represent a substantial improvement over the 1-body models and do correctly assign the polymorphs, it should be noted that the level of discrimination provided here is still small. It seems likely that the assignment is not entirely unique given the expected inherent DFT errors. However, a much larger data set for fragment-based NMR calculations in the solid state is needed before statistical techniques such as a χ^2 test can be applied to assess the robustness of these predictions properly. In any case, given the subtle differences in the spectra in this challenging crystal, it seems unlikely that one could do significantly better with DFT.

Finally, we examine how these chemical shift predictions compare to those one would obtain from periodic GIPAW calculations. Hybrid density functionals such as PBE0 are computationally expensive in a planewave basis, so semilocal

functionals such as PBE are typically used instead. Figure 5 compares the results obtained with GIPAW PBE versus fragment calculations (with charge embedding) for PBE and PBE0. Because direct comparison between Gaussian-type orbitals and plane-wave basis models is difficult, we simply attempted to converge the PBE chemical shielding tensors with respect to the plane-wave cutoff and k-point sampling (see Supporting Information).

The errors for the GIPAW and 2-body fragment PBE calculations are similar, as expected, and both produce the correct polymorph assignment. However, the ~ 2 ppm root-mean-square errors obtained with PBE are about a factor of 2 larger than those found with PBE0, suggesting an advantage to using the hybrid PBE0 functional for this system.

One should also consider the relative computational costs. The fragment method results presented here conservatively included all two-body interactions within 12 Å and used a tightly spaced (150 974) exchange-correlation integration grid. However, equally good results can be obtained with a shorter 6 Å cutoff and a looser (99 590) grid (see Supporting Information). With such parameters, the computational costs of performing PBE functional NMR shielding calculations on sulfanilamide using either the fragment or the GIPAW approach are similar. Switching to the hybrid PBE0 functional instead of PBE increases the fragment method computational time by $\sim 65\%$. In contrast, the nonlocal exchange makes hybrid functionals like PBE0 substantially more expensive to evaluate in a plane-wave basis, and hybrid functionals are rarely used in plane-wave DFT NMR applications.

Of course, the computational costs change dramatically if one opts to include 3-body terms. There are combinatorially many more trimers than dimers within a given set of distance cutoffs, and each one of those trimers takes 3–4 times longer to compute (assuming $O(N^3)$ scaling). In other words, including the trimers can easily increase the overall costs by an order of magnitude or more. Fortunately, 2-body terms appear to be sufficient here.

Overall, fragment methods provide two main potential advantages for computing crystalline chemical shifts at the DFT level. First, they make hybrid functionals routinely applicable to molecular crystal problems. Second, fragment methods become even more efficient in large unit cells because they scale linearly with the number of molecules in the asymmetric unit cell. The cost of the α polymorph ($Z = 8$, $Z' = 1$) is approximately the same as that of the β or γ polymorphs ($Z = 4$, $Z' = 1$), since all three have only one molecule in the asymmetric unit cell. In contrast, a GIPAW calculation on the α polymorph takes several times longer than the same calculation on the smaller β or γ unit cells.

5. CONCLUSION

In conclusion, we have shown that the calculation of NMR chemical shielding tensors in molecular crystals lends itself to a many-body approach. We have illustrated the significant impact of charge embedding at the 1-body level, especially for nitrogen and oxygen, and observed a notable reduction in the utility of charge embedding once higher-order terms in the many body expansion are included. Of course, electrostatic embedding may prove more important in systems where charged functional groups or ions are present. The success of the fragment approach reflects the intrinsically local sensitivity of the chemical shielding tensors to the electronic environment. Capturing the local effects quantum mechanically (i.e., through the 2-body or 3-body

models) using the fragment approach greatly reduces the importance of electrostatic embedding.

The application of these techniques to the drug sulfanilamide provides a proof-of-principle demonstration for the power of fragment-based chemical shift prediction and its potential for use in NMR crystallography as an alternative to the current widespread use of periodic GIPAW-DFT calculations. Despite the subtle differences between polymorphs in the experimental spectra for this challenging species, the calculations correctly assigned these three polymorphs with ~ 1 ppm accuracy in the ^{13}C isotropic chemical shifts.

Although the sulfanilamide calculations here did start from the experimental crystal structures, the atomic positions were fully relaxed with DFT. In other words, one needed only the correct lattice parameters (which can be obtained readily from powder X-ray diffraction) and knowledge of the crystal packing motifs (which can increasingly be obtained from crystal structure prediction techniques^{85–99} and accurate fragment-based lattice energy/structure calculations,^{19,20,26,50,100} especially with the benefit of even limited unit cell information from powder X-ray diffraction).

Several directions merit further study. Most significantly, a major advantage of fragment-based methods is that they enable the application of high-level electronic structure methods to molecular crystals and other complex systems. The results here demonstrate the advantage of using the hybrid PBE0 density functional over the nonhybrid PBE functional for sulfanilamide. Hybrid density functionals are very computationally expensive in plane-wave DFT, but they can be used routinely in fragment based approaches that rely on Gaussian basis sets. Would using methods such as MP2 or potentially even coupled cluster techniques for the NMR calculations improve our ability to discriminate among potential crystal structure assignments? In addition, more crystalline examples are needed to develop a better understanding of the accuracy of these methods and to develop appropriate regression models for converting computed absolute shieldings to relative chemical shifts in the solid state. Research in these directions is currently underway.

■ ASSOCIATED CONTENT

Supporting Information

Structures for the test clusters and sulfanilamide, fragment results for the individual shielding tensor principal components, sulfanilamide linear regression data, and details on the convergence of the crystal calculations with respect to the 2-body and embedding cutoffs. This material is available free of charge via the Internet at <http://pubs.acs.org>.

■ AUTHOR INFORMATION

Corresponding Author

*E-mail: gregory.beran@ucr.edu.

Notes

The authors declare no competing financial interest.

■ ACKNOWLEDGMENTS

Funding for this work from the National Science Foundation (CHE-1362465) and supercomputer time from XSEDE (TG-CHE110064) are gratefully acknowledged. We thank Prof. Robin K. Harris (Durham University) for helpful insights regarding the sulfanilamide experiments and Prof. Bohdan Schatschneider and Stephen Monaco (Penn. State Univ. Fayette) for providing the CASTEP NMR results on sulfanilamide. Finally, we appreciate

numerous helpful discussions with Prof. Leonard Mueller, Thomas Neubauer, Chen Yang (UC Riverside).

REFERENCES

- (1) Salager, E.; Day, G. M.; Stein, R. S.; Pickard, C. J.; Elena, B.; Emsley, L. *J. Am. Chem. Soc.* **2010**, *132*, 2564–2566.
- (2) Baiaş, M.; Widdifield, C. M.; Dumez, J.-N.; Thompson, H. P. G.; Cooper, T. G.; Salager, E.; Bassil, S.; Stein, R. S.; Lesage, A.; Day, G. M.; Emsley, L. *Phys. Chem. Chem. Phys.* **2013**, *15*, 8069–8080.
- (3) Martineau, C.; Senker, J.; Taulelle, F. *Annu. Rep. NMR Spectrosc.* **2014**, *82*, 1–57.
- (4) Pickard, C.; Mauri, F. *Phys. Rev. B* **2001**, *63*, 245101.
- (5) Bonhomme, C.; Gervais, C.; Babonneau, F.; Coelho, C.; Pourpoint, F.; Azais, T.; Ashbrook, S. E.; Griffin, J. M.; Yates, J. R.; Mauri, F.; Pickard, C. *J. Chem. Rev.* **2012**, *112*, 5733–5779.
- (6) Charpentier, T. *Solid State Nucl. Magn. Reson.* **2011**, *40*, 1–20.
- (7) Teale, A. M.; Lutnaes, O. B.; Helgaker, T.; Tozer, D. J.; Gauss, J. J. *Chem. Phys.* **2013**, *138*, 024111.
- (8) Flaig, D.; Maurer, M.; Hanni, M.; Braunger, K.; Kick, L.; Thubauville, M.; Ochsenfeld, C. *J. Chem. Theory Comput.* **2014**, *10*, 572–578.
- (9) Lodewyk, M. W.; Siebert, M. R.; Tantillo, D. J. *Chem. Rev.* **2012**, *112*, 1839–62.
- (10) Johnston, J. C.; Iuliucci, R. J.; Facelli, J. C.; Fitzgerald, G.; Mueller, K. T. *J. Chem. Phys.* **2009**, *131*, 144503.
- (11) Portieri, A.; Harris, R. K.; Fletton, R. A.; Lancaster, R. W.; Threlfall, T. L. *Magn. Reson. Chem.* **2004**, *42*, 313–20.
- (12) Carignani, E.; Borsacchi, S.; Bradley, J. P.; Brown, S. P.; Geppi, M. *J. Phys. Chem. C* **2013**, *117*, 17731–17740.
- (13) Ochsenfeld, C.; Kussmann, J.; Koziol, F. *Angew. Chem., Int. Ed.* **2004**, *43*, 4485–4489.
- (14) Zienau, J.; Kussmann, J.; Ochsenfeld, C. *Mol. Phys.* **2010**, *108*, 333–342.
- (15) Beer, M.; Kussmann, J.; Ochsenfeld, C. *J. Chem. Phys.* **2011**, *134*, 074102.
- (16) Maurer, M.; Ochsenfeld, C. *J. Chem. Phys.* **2013**, *138*, 174104.
- (17) Loibl, S.; Manby, F. R.; Schütz, M. *Mol. Phys.* **2010**, *108*, 477–485.
- (18) Loibl, S.; Schütz, M. *J. Chem. Phys.* **2012**, *137*, 084107.
- (19) Wen, S.; Beran, G. J. O. *Cryst. Growth Des.* **2012**, *12*, 2169–2172.
- (20) Wen, S.; Beran, G. J. O. *J. Chem. Theory Comput.* **2012**, *8*, 2698–2705.
- (21) He, X.; Sode, O.; Xantheas, S. S.; Hirata, S. *J. Chem. Phys.* **2012**, *137*, 204505.
- (22) Hirata, S. *J. Chem. Phys.* **2008**, *129*, 204104.
- (23) Li, J.; Sode, O.; Voth, G. A.; Hirata, S. *Nat. Commun.* **2013**, *4*, 2647.
- (24) Sode, O.; Keceli, M.; Hirata, S.; Yagi, K. *Int. J. Quantum Chem.* **2009**, *109*, 1928–1939.
- (25) Sode, O.; Hirata, S. *Phys. Chem. Chem. Phys.* **2012**, *14*, 7765–7779.
- (26) Hirata, S.; Gilliard, K.; He, X.; Li, J.; Sode, O. *Acc. Chem. Res.* **2014**, *47*, 2721–30.
- (27) He, X.; Wang, B.; Merz, K. M. *J. Phys. Chem. B* **2009**, *113*, 10380–8.
- (28) Gao, Q.; Yokojima, S.; Fedorov, D. G.; Kitaura, K.; M, S.; S, N. J. *Chem. Theory Comput.* **2010**, *6*, 1428–1444.
- (29) Vila, J. A.; Scheraga, H. A. *Acc. Chem. Res.* **2009**, *42*, 1545–53.
- (30) Tang, S.; Case, D. A. *J. Biomol. NMR* **2011**, *51*, 303–12.
- (31) Frank, A.; Onila, I.; Möller, H. M.; Exner, T. E. *Proteins* **2011**, *79*, 2189–202.
- (32) Zhu, T.; He, X.; Zhang, J. Z. H. *Phys. Chem. Chem. Phys.* **2012**, *14*, 7837–45.
- (33) Tan, H.-J.; Bettens, R. P. A. *Phys. Chem. Chem. Phys.* **2013**, *15*, 7541–7.
- (34) Stueber, D. *Concepts Magn. Reson. A* **2006**, *28*, 347–368.
- (35) Ferraro, M. B.; Facelli, J. C. *J. Mol. Struct.* **2002**, *603*, 159–164.
- (36) Zheng, A.; Yang, M.; Yue, Y.; Ye, C.; Deng, F. *Chem. Phys. Lett.* **2004**, *399*, 172–176.
- (37) Chen, X.; Zhan, C.-G. *J. Mol. Struct. (THEOCHEM)* **2004**, *682*, 73–82.
- (38) Zheng, A.; Chen, L.; Yang, J.; Yue, Y.; Ye, C.; Lu, X.; Deng, F. *Chem. Commun.* **2005**, 2474.
- (39) Flaig, D.; Beer, M.; Ochsenfeld, C. *J. Chem. Theory Comput.* **2012**, *8*, 2260–2271.
- (40) Moon, S.; Case, D. A. *J. Comp. Chem.* **2006**, *27*, 825–836.
- (41) Welch, G. W. A.; Karamertzanis, P. G.; Misquitta, A. J.; Stone, A. J.; Price, S. L. *J. Chem. Theory Comput.* **2008**, *4*, 522–532.
- (42) Wen, S.; Nanda, K.; Huang, Y.; Beran, G. J. O. *Phys. Chem. Chem. Phys.* **2012**, *14*, 7578–7590.
- (43) Podeszwa, R.; Rice, B. M.; Szalewicz, K. *Phys. Rev. Lett.* **2008**, *101*, 115503.
- (44) Marom, N.; DiStasio, R. A.; Atalla, V.; Levchenko, S.; Reilly, A. M.; Chelikowsky, J. R.; Leiserowitz, L.; Tkatchenko, A. *Angew. Chem., Int. Ed.* **2013**, *52*, 6629–32.
- (45) Beran, G. J. O. *J. Chem. Phys.* **2009**, *130*, 164115.
- (46) Beran, G. J. O.; Nanda, K. *J. Phys. Chem. Lett.* **2010**, *1*, 3480–3487.
- (47) Wen, S.; Beran, G. J. O. *J. Chem. Theory Comput.* **2011**, *7*, 3733–3742.
- (48) Ditchfield, R. *Mol. Phys.* **1974**, *27*, 789–807.
- (49) Wolinski, K.; Hinton, J. F.; Pulay, P. *J. Am. Chem. Soc.* **1990**, *112*, 8251–8260.
- (50) Nanda, K.; Beran, G. J. O. *J. Chem. Phys.* **2012**, *137*, 174106.
- (51) Stoll, H. *Phys. Rev. B* **1992**, *46*, 6700–6704.
- (52) Stoll, H.; Paulus, B.; Fulde, P. *J. Chem. Phys.* **2005**, *123*, 144108.
- (53) Paulus, B. *Phys. Rep.* **2006**, *428*, 1–52.
- (54) Dahlke, E. E.; Truhlar, D. G. *J. Chem. Theory Comput.* **2007**, *3*, 1342–1348.
- (55) Hermann, A.; Schwerdtfeger, P. *Phys. Rev. Lett.* **2008**, *101*, 183005.
- (56) Kitaura, K.; Ikeo, E.; Asada, T.; Nakano, T.; Uebayasi, M. *Chem. Phys. Lett.* **1999**, *313*, 701–706.
- (57) Fedorov, D. G.; Kitaura, K. *J. Phys. Chem. A* **2007**, *111*, 6904–6914.
- (58) Bygrave, P. J.; Allan, N. L.; Manby, F. R. *J. Chem. Phys.* **2012**, *137*, 164102.
- (59) Goodpaster, J. D.; Barnes, T. A.; Manby, F. R.; Miller, T. F. J. *Chem. Phys.* **2012**, *137*, 224113.
- (60) Stone, A. J. *Chem. Phys. Lett.* **1981**, *83*, 233–239.
- (61) Stone, A. J.; Alderton, M. *Mol. Phys.* **1985**, *56*, 1047–1064.
- (62) Stone, A. J. *J. Chem. Theory Comput.* **2005**, *1*, 1128–1132.
- (63) Misquitta, A. J.; Stone, A. J. *J. Chem. Theory Comput.* **2008**, *4*, 7–18.
- (64) Misquitta, A. J.; Stone, A. J.; Price, S. L. *J. Chem. Theory Comput.* **2008**, *4*, 19–32.
- (65) Beran, G. J. O.; Wen, S.; Nanda, K.; Huang, Y.; Heit, Y. *Top. Curr. Chem.* **2014**, *345*, 59–93.
- (66) Stone, A. J. *The Theory of Intermolecular Forces*; Clarendon Press: Oxford, 2002.
- (67) Tang, K. T.; Toennies, J. P. *J. Chem. Phys.* **1984**, *80*, 3726–3741.
- (68) Frisch, M. J.; Trucks, G. W.; Schlegel, H. B.; Scuseria, G. E.; Robb, M. A.; Cheeseman, J. R.; Scalmani, G.; Barone, V.; Mennucci, B.; Petersson, G. A.; Nakatsuji, H.; Caricato, M.; Li, X.; Hratchian, H. P.; Izmaylov, A. F.; Bloino, J.; Zheng, G.; Sonnenberg, J. L.; Hada, M.; Ehara, M.; Toyota, K.; Fukuda, R.; Hasegawa, J.; Ishida, M.; Nakajima, T.; Honda, Y.; Kitao, O.; Nakai, H.; Vreven, T.; Montgomery, J. A., Jr.; Peralta, J. E.; Ogliaro, F.; Bearpark, M.; Heyd, J. J.; Brothers, E.; Kudin, K. N.; Staroverov, V. N.; Kobayashi, R.; Normand, J.; Raghavachari, K.; Rendell, A.; Burant, J. C.; Iyengar, S. S.; Tomasi, J.; Cossi, M.; Rega, N.; Millam, J. M.; Klene, M.; Knox, J. E.; Cross, J. B.; Bakken, V.; Adamo, C.; Jaramillo, J.; Gomperts, R.; Stratmann, R. E.; Yazyev, O.; Austin, A. J.; Cammi, R.; Pomelli, C.; Ochterski, J. W.; Martin, R. L.; Morokuma, K.; Zakrzewski, V. G.; Voth, G. A.; Salvador, P.; Dannenberg, J. J.; Dapprich, S.; Daniels, A. D.; Farkas, O.; Foresman, J. B.; Ortiz, J. V.; Cioslowski, J.; Fox, D. J. *Gaussian 09*, revision A.1; Gaussian, Inc.: Wallingford, CT, 2009.
- (69) Adamo, C.; Barone, V. *J. Chem. Phys.* **1999**, *110*, 6158.
- (70) Krishnan, R.; Binkley, J. S.; Seeger, R.; Pople, J. A. *J. Chem. Phys.* **1980**, *72*, 650–654.
- (71) McLean, A. D.; Chandler, G. S. *J. Chem. Phys.* **1980**, *72*, 5639–5648.

- (72) Frisch, M. J.; Pople, J. A.; Binkley, J. S. *J. Chem. Phys.* **1984**, *80*, 3265–3269.
- (73) Clark, T.; Chandrasekhar, J.; Spitznagel, G. W.; v. R. Schleyer, P. J. *Comput. Chem.* **1983**, *4*, 294–301.
- (74) Misquitta, A. J.; Stone, A. J. CamCASP v5.6 (2011), <http://www-stone.ch.cam.ac.uk/programs.html> (accessed Feb. 23, 2011).
- (75) Stone, A. J. *GDMA, Distributed Multipole Analysis of Gaussian Wavefunctions*, version 2.2.09; <http://www-stone.ch.cam.ac.uk/pub/gdma/> (accessed May 28, 2014).
- (76) Tozer, D. J.; Handy, N. C. *J. Chem. Phys.* **1998**, *109*, 10180–10189.
- (77) Tozer, D. J. *J. Chem. Phys.* **2000**, *112*, 3507–3515.
- (78) Dunning, T. H. *J. Chem. Phys.* **1989**, *90*, 1007–1023.
- (79) Sadlej, A. J. *Collect. Czech. Chem. Commun.* **1988**, *53*, 1995–2016.
- (80) Sadlej, A. J. *Theor. Chim. Acta* **1991**, *79*, 123–140.
- (81) Sebetci, A.; Beran, G. J. O. *J. Chem. Theory Comput.* **2010**, *6*, 155–167.
- (82) Perdew, J. P.; Burke, K.; Ernzerhof, M. *Phys. Rev. Lett.* **1996**, *77*, 3865.
- (83) Clark, S. J.; Segall, M. D.; Pickard, C. J.; Hasnip, P. J.; Probert, M. I.; Refson, K.; Payne, M. C. *Z. Kristallogr.* **2005**, *220*, 567–570.
- (84) Monaco, S.; Schatschneider, B. private communication, 2014.
- (85) Becke, A. D. *J. Chem. Phys.* **1993**, *98*, 5648–5652.
- (86) Civalieri, B.; Zicovich-Wilson, C. M.; Valenzano, L.; Ugliengo, P. *CrystEngComm* **2008**, *10*, 405–410.
- (87) Schafer, A.; Horn, H.; Ahlrichs, R. *J. Chem. Phys.* **1992**, *97*, 2571.
- (88) Dovesi, R.; Orlando, R.; Civalieri, B.; Roetti, C.; Saunders, V. R.; Zicovich-Wilson, C. M. *Z. Kristallogr.* **2005**, *220*, 571–573.
- (89) Dovesi, R.; Saunders, V. R.; Roetti, C.; Orlando, R.; Zicovich-Wilson, C. M.; Pascale, F.; Civalieri, B.; Doll, K.; Harrison, N. M.; Bush, I. J.; D'Arco, P.; Llunell, M. *CRYSTAL09 User's Manual*; University of Torino: Torino, 2009.
- (90) Haeberlen, U. *High Resolution NMR in Solids*. In *Advances in Magnetic Resonance, Supplement 1*; Waugh, J. S., Ed.; Academic Press: New York, 1976.
- (91) Mehring, M. *Principles of High Resolution NMR in Solids*, 2nd ed.; Springer Verlag: Berlin, 1983.
- (92) Spiess, H. W. *Dynamic NMR Spectroscopy*. In *NMR: Basic Principles and Progress*; Diehl, P., Fluck, E., Kosfeld, R., Eds.; Springer Verlag: New York, 1978; Vol. 15.
- (93) Gelbrich, T.; Bingham, A. L.; Threlfall, T. L.; Hursthouse, M. B. *Acta Cryst. C* **2008**, *64*, o205–o207.
- (94) Morcombe, C. R.; Zilm, K. W. *J. Magn. Reson.* **2003**, *162*, 479–486.
- (95) Day, G. M.; et al. *Acta Cryst. B* **2009**, *65*, 107–25.
- (96) Neumann, M. A.; Leusen, F. J. J.; Kendrick, J. *Angew. Chem., Int. Ed.* **2008**, *47*, 2427–2430.
- (97) Bardwell, D. A.; et al. *Acta Cryst. B* **2011**, *67*, 535–51.
- (98) Kazantsev, A. V.; Karamertzanis, P. G.; Adjiman, C. S.; Pantelides, C. C.; Price, S. L.; Galek, P. T. A.; Day, G. M.; Cruz-Cabeza, A. J. *Int. J. Pharm.* **2011**, *418*, 168–178.
- (99) Kendrick, J.; Leusen, F. J. J.; Neumann, M. A.; van de Streek, J. *Chem.—Eur. J.* **2011**, *17*, 10736–10744.
- (100) Gillan, M. J.; Alfè, D.; Bygrave, P. J.; Taylor, C. R.; Manby, F. R. *J. Chem. Phys.* **2013**, *139*, 114101.